

Re: Voltage-Sourced Converters in Power Systems, ISBN: 978-0-470-52156-4

Dear researcher,

The following pages indicate the errors that have been overlooked during the final production stage of the book. Please fix the errors in your copy.

We will try to continuously update this document and thus appreciate if you could bring to our attention any errors that are not included in this file.

Thanks

A. Yazdani

R. Iravani

Last updated June 15, 2011

interfaced with each other, that is, without power-electronic converters. For instance, a power-electronic converter is required to interface a wind turbine/generator unit, that is, an electromechanical subsystem that generates a variable-frequency/variable-voltage electricity, with the constant-frequency/constant-voltage utility grid, that is, another electromechanical subsystem.

In the technical literature, converters are commonly categorized based on the type of electrical subsystems, that is, AC or DC, that they interface. Thus,

- A DC-to-AC or DC/AC converter interfaces a DC subsystem to an AC subsystem.
- A DC-to-DC or DC/DC converter interfaces two DC subsystems.
- An AC-to-AC or AC/AC converter interfaces two AC subsystems.

Based on the foregoing classification, a DC/AC converter is equivalent to an AC/DC converter. Hence, in this book, the terms DC/AC converter and AC/DC converter are used interchangeably. The conventional diode-bridge rectifier is an example of a DC/AC converter. A DC/AC converter is called a *rectifier* if the flow of average power is from the AC side to the DC side. Alternatively, the converter is called an *inverter* if the average power flow is from the DC side to the AC side. Specific classes of DC/AC converters provide bidirectional power-transfer capability, that is, they can operate either as a rectifier or as an inverter. Other types, for example, the diode-bridge converter, can only operate as a rectifier.

DC/DC converter and AC/AC converter are also referred to as *DC converter* and *AC converter*, respectively. A DC converter can directly interface two DC subsystems, or it can employ an intermediate AC link. In the latter case, the converter is composed of two back-to-back DC/AC converters which are interfaced through their AC sides. Similarly, an AC converter can be direct, for example, the matrix converter, or it can employ an intermediate DC link. The latter type consists of two back-to-back DC/AC converters which are interfaced through their DC sides. This type is also known as *AC/DC/AC converter*, which is widely used in AC motor drives and variable-speed wind-power conversion units. *and*

In this book, we define a *power-electronic converter system* (or a converter system) as a composition of one (or more) power-electronic converter(s) and a control/protection scheme. The link between the converter(s) and the control/protection scheme is established through gating signals issued for semiconductor switches, and also through feedback signals. Thus, the transfer of energy in a converter system is accomplished through appropriate switching of the semiconductor switches by the control scheme, based on the overall desired performance, the supervisory commands, and the feedback from a multitude of system variables.

This book concentrates on modeling and control of a specific class of converter systems, ~~this~~ *that* is, the VSC systems. This class is introduced in Section 1.6.

diodes are extensively used in power-electronic converter circuits as stand-alone components, and/or as integral parts of other switches.

1.4.1.2 Semicontrollable Switches The most widely used semicontrollable electronic switch is the thyristor or the silicon-controlled rectifier (SCR). The thyristor is a four-layer semiconductor device that is half- or semicontrollable, since only the instant at which its current conduction starts can be determined by a gating signal, provided that the device is properly voltage biased. However, the current interruption instant of the thyristor is determined by the host electrical circuit. The thyristor has been, and even currently is, the switch of choice for HVDC converters, although in recent years fully controllable switches have also been considered and utilized for HVDC applications.

1.4.1.3 Fully Controllable Switches The current conduction and interruption instants of a fully controllable switch can be determined by means of a gating command. Most widely used fully controllable switches include

The most

- *Metal-Oxide-Semiconductor Field-Effect Transistor (MOSFET)*: The MOSFET is a three-layer semiconductor device. Compared to other fully controllable power switches, current and voltage ratings of power MOSFETs are fairly limited. Consequently, the application of power MOSFETs is confined to relatively lower power converters where a high switching frequency is the main requirement.
- *Insulated-Gate Bipolar Transistor (IGBT)*: The IGBT is also a three-layer semiconductor device. The power IGBT has significantly evolved since the early 1990s, in terms of the switching frequency, the current rating, and the voltage rating. At present, it is used for a broad spectrum of applications in electric power systems.
- *Gate-Turn-Off Thyristor (GTO)*: The GTO is structurally a four-layer semiconductor device and can be turned on and off by external gating signals. The GTO requires a relatively large, negative current pulse to turn off. This requirement calls for an elaborate and lossy drive scheme. Among the fully controllable switches, the GTO used to be the switch of choice for high-power applications in the late 1980s and early 1990s. However, it has lost significant ground to the IGBT in the last several years.
- *Integrated Gate-Commutated Thyristor (IGCT)*: The IGCT conceptually and structurally is a GTO switch with mitigated turn-off drive requirements. In addition, the IGCT has a lower on-state voltage drop and can also be switched faster compared to the GTO. In recent years, the IGCT has gained considerable attention for high-power converters due to its voltage/current handling capabilities.

In terms of voltage/current handling capability, the semicontrollable and fully controllable switches are classified as follows:

Q_1 carries i (Fig. 2.14(d)), and

$$V'_t = V_p - r_{on}i - V_d. \quad (2.32)$$

Note that the term $r_{on}i + V_d$ is considerably smaller than V_p and therefore $V'_t \approx V_p = V_{DC}/2$, as Figure 2.14(c) indicates. At $t = dT_s$, the gating command of Q_1 is removed and i_{Q1} rapidly drops to its tailing current level (Fig. 2.14(d)). Therefore, D_4 starts conducting, and i_{D4} increases rapidly (Fig. 2.14(e)). The tailing current process lasts for t_{tc} until the whole tailing current charge of Q_{tc} is removed from the transistor. During the tailing current process, the following equation holds:

$$\begin{aligned} V'_t &= V_n - r_{on}i_{D4} - V_d \\ &= V_n - r_{on}(i - i_{Q1}) - V_d, \end{aligned} \quad (2.33)$$

and $V'_t \approx -V_{DC}/2$ (Fig. 2.14(c)). At $t = dT_s + t_{tc}$, i_{Q1} becomes zero and $i_{D4} = i$, as Figure 2.14(e) illustrates. From $t = dT_s + t_{tc}$ to T_s , the whole AC-side current is carried by D_4 , and we have

$$V'_t = V_n - r_{on}i - V_d, \quad (2.34)$$

and $V'_t \approx -V_{DC}/2$, as Figure 2.14(c) shows.

The average of the AC-side terminal voltage is

$$\begin{aligned} \overline{V'_t} &= \frac{1}{T_s} \int_0^{T_s} V'_t(\tau) d\tau \\ &= \frac{1}{T_s} \left(\int_0^{t_{rr}} V'_t d\tau + \int_{t_{rr}}^{dT_s} V'_t d\tau + \int_{dT_s}^{dT_s+t_{tc}} V'_t d\tau + \int_{dT_s+t_{tc}}^{T_s} V'_t d\tau \right), \end{aligned} \quad (2.35)$$

where V'_t , for each time interval, is obtained from (2.31) to (2.34), respectively. Substituting for V'_t in (2.35), based on (2.31)–(2.34), knowing that $\int_0^{t_{rr}} i_{D4}(\tau) d\tau = -Q_{rr}$ and $\int_{dT_s}^{dT_s+t_{tc}} i_{Q1} d\tau = Q_{tc}$, and rearranging the result, we conclude that

$$\begin{aligned} \overline{V'_t} &= m \frac{V_{DC}}{2} - V_e - r_e i \\ &= \overline{V}_t - V_e - r_e i, \quad \text{for } i > 0, \end{aligned} \quad (2.36)$$

where $\overline{V}_t = m V_{DC}/2$ based on (2.26), and

$$V_e = V_d - \left(\frac{Q_{rr} + Q_{tc}}{T_s} \right) r_{on} + V_{DC} \left(\frac{t_{rr}}{T_s} \right), \quad (2.37)$$

$$r_e = \left(1 - \frac{t_{rr}}{T_s} \right) r_{on}. \quad (2.38)$$

step function and V_s is a DC voltage, a proportional-integral (PI) compensator of the generic form $K(s) = (k_p s + k_i)/s$ is sufficient for the control. The integral term of the compensator guarantees that i tracks i_{ref} , with zero steady-state error, in spite of the disturbance V_s .

As understood from Figure 3.3, if $K(s) = (k_p s + k_i)/s$, the control system loop gain is

$$\ell(s) = \left(\frac{k_p}{Ls} \right) \left(\frac{s + \frac{k_i}{k_p}}{s + \frac{R+r_{on}}{L}} \right). \quad (3.3)$$

Based on the block diagrams of Figures 3.2 and 3.3, the open-loop half-bridge converter has a stable pole at $p = -(R + r_{on})/L$. Typically, this pole is fairly close to the origin and corresponds to a slow natural response. To improve the open-loop frequency response, the pole can be canceled by the zero of the PI compensator. Thus, choosing $k_i/k_p = (R + r_{on})/L$ and $k_p/L = 1/\tau_i$, where τ_i is the desired time constant of the closed-loop system, one obtains the closed-loop transfer function

$$G_i(s) = \frac{\mathbf{I}(s)}{\mathbf{I}_{ref}(s)} = \frac{1}{\tau_i s + 1}, \quad (3.4)$$

which is a first-order transfer function with the unity gain. τ_i should be made small for a fast current-control response, but adequately large such that $1/\tau_i$, that is, the bandwidth of the closed-loop control system, is considerably smaller, for example, 10 times smaller, than the switching frequency of the half-bridge converter (expressed in rad/s). Depending on the requirements of a specific application and the converter switching frequency, τ_i is typically selected in the range of 0.5–5 ms.

Example 3.1 illustrates the performance of the current-controlled half-bridge converter in tracking a step command.

EXAMPLE 3.1 Closed-Loop Response of the Half-Bridge Converter

Consider the half-bridge converter of Figure 3.1 with parameters $L = 690 \mu\text{H}$, $R = 5 \text{ m}\Omega$, $r_{on} = 0.88 \text{ m}\Omega$, $V_d = 1.0 \text{ V}$, $V_{DC}/2 = 600 \text{ V}$, $V_s = 400 \text{ V}$, and $f_s = 1620 \text{ Hz}$. To achieve a closed-loop time constant of 5 ms, the compensator parameters are chosen as $k_p = 0.138 \Omega$ and $k_i = 1.176 \Omega/\text{s}$.

Initially, the half-bridge converter system is in a steady state and $i = 0$. The current command, i_{ref} , is first changed from 0 to 1000 A, at $t = 0.1 \text{ s}$, and then changed from 1000 to -1000 A , at $t = 0.2 \text{ s}$. These correspond to changes in the AC-side power from 0 to 400 kW and from 400 to -400 kW , respectively. Figure 3.4(a)–(d) shows the half-bridge converter response to the step changes in i_{ref} . Figure 3.4(a) shows the compensator response to the command changes. The response of the compensator output u is equivalent to that of the AC-side terminal voltage V_t , required for the command tracking. u is then translated into the modulating waveform m (Fig. 3.4(b)), which is rendered to the converter PWM scheme. As expected, the step response of i is a first-order exponential

a very small closed-loop time constant may not be possible due to practical limitations/requirements. For example, while a closed-loop current controller with a time constant of $\tau_i = 2$ ms is considered as being reasonably fast for most high-power converter systems, it tracks a 60 Hz sinusoidal command with an amplitude attenuation of 20% and a phase delay of 37° .

Example 3.5 illustrates the sinusoidal command following performance of the half-bridge converter system if a PI compensator is used.

EXAMPLE 3.5 Sinusoidal Command Following with PI Compensator

Consider the half-bridge converter of Figure 3.1, in conjunction with the control scheme of Figure 3.6, with the following parameters: $L = 690 \mu\text{H}$, $R = 5 \text{ m}\Omega$, $r_{on} = 0.88 \text{ m}\Omega$, $V_d = 1.0 \text{ V}$, $V_{DC}/2 = 600 \text{ V}$, and $f_s = 3420 \text{ Hz}$. The compensator parameters are $k_p = 0.345 \Omega$ and $k_i = 2.94 \Omega/\text{s}$, which correspond to $\tau_i = 2 \text{ ms}$. The transfer function of the feed-forward filter is $G_{ff}(s) = 1/(8 \times 10^{-6}s + 1)$.

Let us assume that $V_s = 400 \cos(377t - \frac{\pi}{2}) \text{ V}$ and that we intend to deliver 200 kW to the AC system, at unity power factor. Thus, the current command $i_{ref} = 1000 \cos(377t - \frac{\pi}{2}) \text{ A}$ must be tracked by the closed-loop converter system. Figure 3.15 shows the system closed-loop response to i_{ref} when a PI compensator is employed. As Figure 3.15 illustrates, $i(t)$ is about 37° delayed with respect to $i_{ref}(t)$ and $V_s(t)$. Moreover, the amplitude of i is only about 800 A. Consequently, rather than 200 kW at unity power factor, 128 kW and 96 kVAr are delivered to the AC-side source.

To further investigate the mechanism of the time-varying command tracking, consider the closed-loop control system of Figure 3.16 with the transfer function

$$\frac{I(s)}{I_{ref}(s)} = G_i(s) = \frac{\ell(s)}{1 + \ell(s)}, \quad (3.9)$$

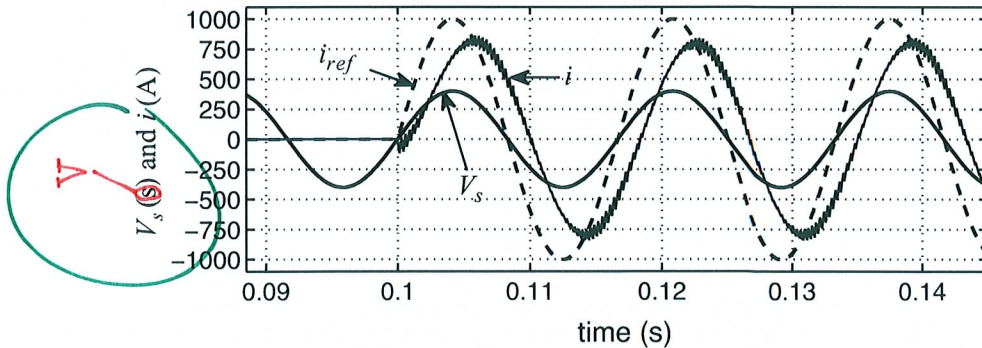


FIGURE 3.15 Steady-state error in phase and amplitude of the current when PI compensator is employed; Example 3.5.

adequately larger than the frequency of the command signal. In this approach, no attempt is usually made to include the unstable poles of the command signal in the compensator. Consequently, the tracking will not be perfect and a steady-state error, although small, is inevitable. The design procedure is almost the same in both methods and illustrated by Example 3.6.

EXAMPLE 3.6 Sinusoidal Command Following with a Modified Compensator

Consider the half-bridge converter of Example 3.5 and the control block diagram of Figure 3.6. Let us assume that i_{ref} is required to be tracked with zero steady-state error and that a closed-loop bandwidth of about 3500 rad/s (i.e., about 9 times ω_0) is desired.

To satisfy the zero steady-state error requirement, we include a pair of complex-conjugate poles in the compensator, at $s = \pm 377j$ rad/s. Thus, a candidate compensator is $K(s) = (s^2 + (377)^2)^{-1} H(s)$, where $H(s) = h(N(s)/D(s))$ is a rational fraction of the polynomials $N(s)$ and $D(s)$, and h is a constant.² The compensator zeros ~~X~~ and the other poles (if required) must be located in the s plane such that the closed-loop system is stable, a reasonable phase margin is achieved, and the switching ripple content of the control signal u is low. The compensator can be designed based on either the root-locus method or the frequency-response approach. For this example, we adopt the frequency-response method (also known as the *loop shaping*).

If $H(j\omega) = 1$, that is, $K(j\omega) = [-\omega^2 + (377)^2]^{-1}$, the magnitude and phase plots of $\ell(j\omega) = K(j\omega)G(j\omega) = K(j\omega)[jL\omega + (R + r_{on})]^{-1}$ assume the shapes shown by dashed lines in Figure 3.17. It is observed that at very low frequencies $\ell(j\omega)$ has a constant magnitude, and the phase delay is insignificant. However, due to the open-loop pole $s = -(R + r_{on})/L$, the magnitude starts to roll off at about $\omega = 8.52$ rad/s. The pole also results in a phase drop with a slope of $-45^\circ/\text{dec}$, such that the phase settles at -90° for frequencies larger than 85 rad/s. At $\omega = 377$ rad/s, that is, the resonance frequency of the complex-conjugate poles, the loop-gain magnitude peaks to infinity but continues to roll off with a slope of -60 dB/dec. The resonance also results in a -180° phase delay, such that the loop-gain phase drops to -270° , for frequencies larger than 377 rad/s.

To achieve a stable closed-loop system, one must ensure that the loop-gain phase at the gain crossover frequency is larger than -180° , by a value that is referred to as the *phase margin*. The gain crossover frequency, denoted by ω_c , is the frequency at which the loop-gain magnitude becomes unity (0 dB) [37]. On the other hand, the gain crossover frequency and the -3 dB bandwidth of the closed-loop system, denoted by ω_b , are closely correlated, such that, in general, ω_b satisfies the inequality $\omega_c < \omega_b < 2\omega_c$ and can be approximated as $\omega_b \approx 1.5\omega_c$. Therefore, ω_c is imposed if a certain value is required for ω_b . In this

² $N(s)$ and $D(s)$ are arranged such that the coefficients of their highest order terms are unity.

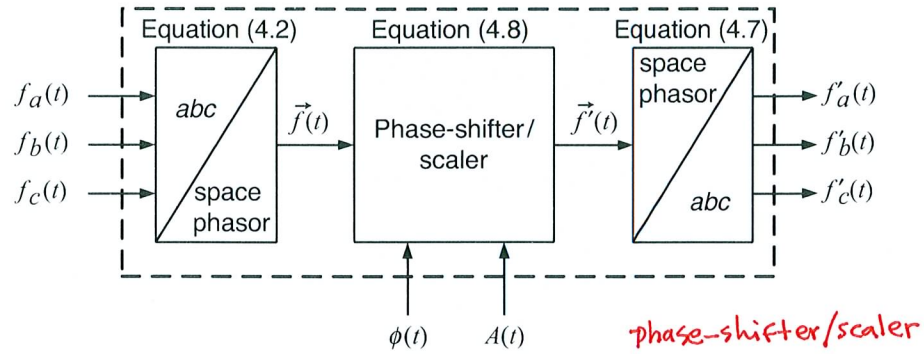


FIGURE 4.5 Block diagram of the modified space-phaser phase shifter/scaler.

AC-side terminal voltage, V_{t-abc} , relative to those of the AC system voltage, V_{s-abc} [46, 47]. Thus, $\phi(t)$ ($A(t)$) is commanded by a (another) feedback loop that processes the error between the real power (reactive power) and its respective reference value, to regulate the real power (reactive power). The output of the space-phaser phase-shifter/scaler corresponds to the terminal voltage to be reproduced by the VSC and is delivered to the VSC pulse-width modulation (PWM) switching scheme.

Example 4.1 illustrates the operation of the space-phaser phase-shifter/scaler of Figure 4.4.

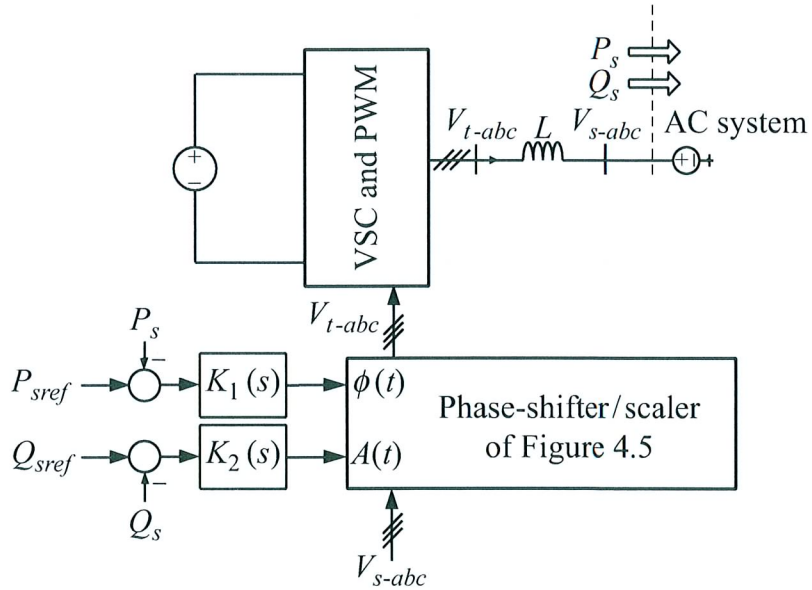


FIGURE 4.6 Block diagram of voltage-controlled VSC system.

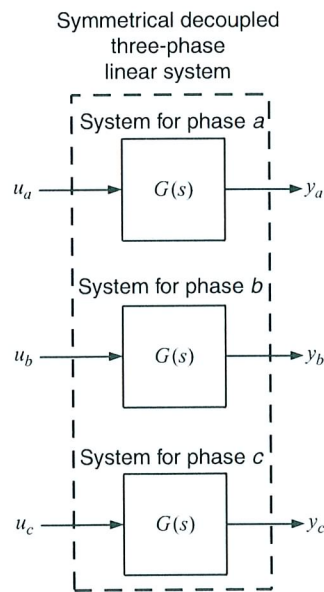
TABLE 4.1 Positive- and Negative-Sequence Harmonics

Positive-Sequence Harmonic $\vec{f}_n(t) = \hat{f}_n e^{jn\omega t}$	Negative-Sequence Harmonic $\vec{f}_n(t) = \hat{f}_n e^{-jn\omega t}$
$n = 1$	$n = 2$
4	5
7	8
10	11
13	14
16	17
19	20
22	23
25	26
28	29
31	32

we identify three classes of three-phase systems: symmetrical and decoupled, symmetrical and coupled, and asymmetrical.

4.3.1 Decoupled Symmetrical Three-Phase Systems

Consider the three-phase system of Figure 4.13 in which each phase of the output y_{abc} is controlled by the corresponding phase of the input u_{abc} . The system of Figure 4.13 is composed of three decoupled identical subsystems. The system is symmetrical since the input/output relationships of the three phases retain their original expressions if

**FIGURE 4.13** Block diagram of a symmetrical, decoupled, linear, three-phase system.

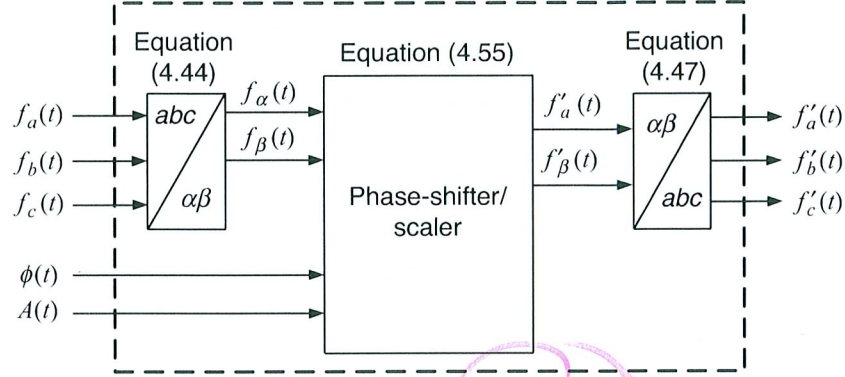


FIGURE 4.22 Block diagram of a space-phasor phase-shifter/scaler in $\alpha\beta$ -frame, equivalent to Figure 4.5

$i_\alpha - ji_\beta$, and obtain

$$P(t) = \frac{3}{2} [v_\alpha(t)i_\alpha(t) + v_\beta(t)i_\beta(t)] \quad (4.56)$$

and

$$Q(t) = \frac{3}{2} [-v_\alpha(t)i_\beta(t) + v_\beta(t)i_\alpha(t)]. \quad (4.57)$$

4.5.4 Control in $\alpha\beta$ -Frame

Figure 4.24 illustrates the generic control block diagram of a three-phase VSC system in $\alpha\beta$ -frame. The control plant may consist of three-phase electric machines, VSCs,

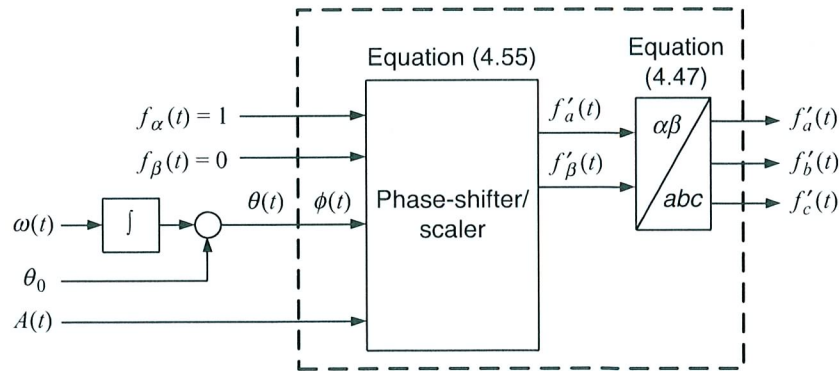


FIGURE 4.23 Block diagram of a controllable-frequency/amplitude three-phase signal generator in $\alpha\beta$ -frame, equivalent to Figure 4.10.

To highlight the usefulness of the transformation given by (4.65), assume that \vec{f} has the following general form:

$$\vec{f}(t) = f_\alpha + jf_\beta = \hat{f}(t)e^{j[\theta_0 + \int \omega(\tau)d\tau]},$$

where $\omega(t)$ is the (time-varying) frequency and θ_0 is the initial phase angle of the three-phase signal corresponding to $\vec{f}(t)$. If $\varepsilon(t)$ is chosen as

$$\varepsilon(t) = \varepsilon_0 + \int \omega(\tau)d\tau,$$

then based on (4.65) the dq -frame representation of $\vec{f}(t)$ becomes

$$f_d + jf_q = \hat{f}(t)e^{j(\theta_0 - \varepsilon_0)},$$

which is stationary and, therefore, the constituents of its corresponding three-phase signal are DC quantities. Note that $\theta(t)$ and $\varepsilon(t)$ are not necessarily equal, but $d\theta(t)/dt = d\varepsilon(t)/dt$ must be ensured.

To better describe the dq -frame transformation, let us rewrite (4.66) as

$$\vec{f} = f_d(1 + 0 \cdot j)e^{j\varepsilon(t)} + f_q(0 + 1 \cdot j)e^{j\varepsilon(t)}. \quad (4.67)$$

An interpretation of (4.67) is that the vector \vec{f} is represented by its components, that is, f_d and f_q , in an orthogonal coordinate system whose axes are along the unit vectors $(1 + 0 \cdot j)e^{j\varepsilon(t)}$ and $(0 + 1 \cdot j)e^{j\varepsilon(t)}$. In turn, $(1 + 0 \cdot j)$ and $(0 + 1 \cdot j)$ are the unit vectors along the α -axis and the β -axis of the $\alpha\beta$ -frame, respectively. Therefore, as illustrated in Figure 4.26, one can consider \vec{f} as a vector represented by the components f_d and f_q in a coordinate system that is rotated by $\varepsilon(t)$ with respect to the $\alpha\beta$ -frame. We refer to this rotated coordinate system as **a** dq -frame. For the reason given above, the dq -frame is also known as *rotating reference frame*, in the technical literature. Usually, the rotational speed of the dq -frame is selected to be equal to that of \vec{f} .

Based on the Euler's identity $e^{j(\cdot)} = \cos(\cdot) + j \sin(\cdot)$, (4.65) can be written as

$$\begin{bmatrix} f_d(t) \\ f_q(t) \end{bmatrix} = \mathbf{R}[\varepsilon(t)] \begin{bmatrix} f_\alpha(t) \\ f_\beta(t) \end{bmatrix}, \quad (4.68)$$

where

$$\mathbf{R}[\varepsilon(t)] = \begin{bmatrix} \cos \varepsilon(t) & \sin \varepsilon(t) \\ -\sin \varepsilon(t) & \cos \varepsilon(t) \end{bmatrix}. \quad (4.69)$$

A direct transformation from the abc -frame to the dq -frame can be obtained by substitution of $[f_\alpha \ f_\beta]^T$ from (4.44) in (4.68), as

$$\begin{bmatrix} f_d(t) \\ f_q(t) \end{bmatrix} = \frac{2}{3} \mathbf{T}[\varepsilon(t)] \begin{bmatrix} f_a(t) \\ f_b(t) \\ f_c(t) \end{bmatrix}, \quad (4.73)$$

where

$$\mathbf{T}[\varepsilon(t)] = \mathbf{R}[\varepsilon(t)]\mathbf{C} = \begin{bmatrix} \cos[\varepsilon(t)] & \cos\left[\varepsilon(t) - \frac{2\pi}{3}\right] & \cos\left[\varepsilon(t) - \frac{4\pi}{3}\right] \\ \sin[\varepsilon(t)] & \sin\left[\varepsilon(t) - \frac{2\pi}{3}\right] & \sin\left[\varepsilon(t) - \frac{4\pi}{3}\right] \end{bmatrix}, \quad (4.74)$$

Similarly, a direct transformation from the dq -frame to the abc -frame can be obtained by substituting for $[f_\alpha \ f_\beta]^T$ from (4.70) in (4.47) as

$$\begin{bmatrix} f_a(t) \\ f_b(t) \\ f_c(t) \end{bmatrix} = \mathbf{T}[\varepsilon(t)]^T \begin{bmatrix} f_d(t) \\ f_q(t) \end{bmatrix}, \quad (4.75)$$

where

$$\mathbf{T}[\varepsilon(t)]^T = \mathbf{C}^T \mathbf{R}[-\varepsilon(t)] = \begin{bmatrix} \cos[\varepsilon(t)] & \sin[\varepsilon(t)] \\ \cos\left[\varepsilon(t) - \frac{2\pi}{3}\right] & \sin\left[\varepsilon(t) - \frac{2\pi}{3}\right] \\ \cos\left[\varepsilon(t) - \frac{4\pi}{3}\right] & \sin\left[\varepsilon(t) - \frac{4\pi}{3}\right] \end{bmatrix}. \quad (4.76)$$

Based on Figure 4.26, one deduces

$$\hat{f}(t) = \sqrt{f_d^2(t) + f_q^2(t)}, \quad (4.77)$$

$$\cos[\delta(t)] = \frac{f_d(t)}{\hat{f}(t)} = \frac{f_d(t)}{\sqrt{f_d^2(t) + f_q^2(t)}}, \quad (4.78)$$

$$\sin[\delta(t)] = \frac{f_q(t)}{\hat{f}(t)} = \frac{f_q(t)}{\sqrt{f_d^2(t) + f_q^2(t)}}, \quad (4.79)$$

$$\theta(t) = \varepsilon(t) + \delta(t). \quad (4.80)$$

$$\begin{aligned}
f_{a0} &= \frac{m_0 \hat{i}}{2\pi} \left(\int_0^{\pi/2} \cos(\theta - \gamma) d\theta - \int_{\pi/2}^{3\pi/2} \cos(\theta - \gamma) d\theta + \int_{3\pi/2}^{2\pi} \cos(\theta - \gamma) d\theta \right) \\
&\quad + \frac{\hat{m} \hat{i}}{4\pi} \cos \gamma \left(\int_0^{\pi/2} d\theta - \int_{\pi/2}^{3\pi/2} d\theta + \int_{3\pi/2}^{2\pi} d\theta \right) \\
&\quad + \frac{\hat{m} \hat{i}}{4\pi} \left(\int_0^{\pi/2} \cos(2\theta - \gamma) d\theta - \int_{\pi/2}^{3\pi/2} \cos(2\theta - \gamma) d\theta + \int_{3\pi/2}^{2\pi} \cos(2\theta - \gamma) d\theta \right) \\
&= \frac{2\hat{i} \cos \gamma}{\pi} m_0.
\end{aligned} \tag{6.57}$$

Substituting for f_{a0} from (6.57) in (6.53), one concludes

$$i_{np0}(t) = -\frac{6\hat{i} \cos \gamma}{\pi} m_0(t). \tag{6.58}$$

Equation (6.58) suggests that the DC component of i_{np} can be controlled by m_0 . Based on (6.58), the control transfer function is linear, but with a variable gain. The gain is zero if either the three-level NPC AC-side current is small or the converter operates at zero power factor. However, the gain is the largest if the three-level NPC operates at its rated capacity and unity power factor.

To equalize the DC components of the two DC-side voltages, a closed-loop scheme compares them and controls m_0 [61, 65]. Figure 6.15 shows a circuit model of the DC-side voltages and the midpoint current in which partial DC-side voltages are denoted by V_1 and V_2 . Figure 6.15 indicates that i_{np} has two components: a third-harmonic component, i_{np3} , and a DC component, i_{np0} , which are formulated by (6.45) and (6.58), respectively. As an approximation, we assume that the capacitors are identical, each with a capacitance of $2C$.

If V_{DC} , that is, the net DC-side voltage, has no third-harmonic component, it can be replaced by a short circuit. Thus, the circuit of Figure 6.15 is simplified to the equivalent circuit of Figure 6.16(a), for the third-harmonic component. Based on Figure 6.16(a) and since the capacitors are identical, i_{np3} is equally divided between the two capacitors, and $i_1 = -i_2 = i_{np3}/2$, where i_{np3} is expressed by (6.45). Hence, in a steady state, the third-order harmonic components of V_1 and V_2 are given by

$$\langle V_1 \rangle_3 = \hat{V}_{r3} \sin(3\omega t + \zeta) \tag{6.59}$$

$$\langle V_2 \rangle_3 = -\hat{V}_{r3} \sin(3\omega t + \zeta), \tag{6.60}$$

where $\omega = d\varepsilon/dt$ and $\zeta = \pi - \tan^{-1}(1.5 \tan \gamma)$, and the peak voltage ripple \hat{V}_{r3} is

$$\hat{V}_{r3} = \frac{\hat{m} \hat{i}}{15\pi C \omega} \sqrt{9 - 5 \cos^2 \gamma}. \tag{6.61}$$

be a proper transfer function.⁴ The following example demonstrates the design procedure.

EXAMPLE 7.3 Real-/Reactive-Power Controller Based on the Three-level NPC

Consider the VSC system of Figure 7.12 that utilizes the three-level NPC of Figure 7.14 and adopts the third-harmonic injected PWM strategy. The system parameters and controllers are the same as those in Example 7.1, except that $2C = 19250 \mu\text{F}$, $r_{on} = 0.44 \text{ m}\Omega$, and $V_{DC} = 1.25 \text{ kV}$. The rated power of the system of Figure 7.12 is $P_s = 1.0 \text{ MW}$. Based on $\hat{m} = 2\hat{V}_t/V_{DC}$ and assuming $\hat{V}_t \approx \hat{V}_s = 0.391 \text{ kV}$, we obtain $\hat{m} \approx 0.63$. Thus, the plant transfer function, in the closed-loop system of Figure 7.16, is

$$G(s) = \left(\frac{4}{\pi C V_{DC} \hat{m}} \right) \frac{1}{s} = \frac{168}{s} \quad [(\text{kA})^{-1}].$$

Let $F(s)$ be

$$F(s) = \frac{s^2 + (3\omega_0)^2}{(s + 3\omega_0)^2} = \frac{s^2 + 1131^2}{s^2 + 2262s + 1131^2},$$

where $\omega_0 = 377 \text{ rad/s}$. Then, (i) the third-harmonic component of $V_1 - V_2$ is suppressed, (ii) $F(s)$ has a unity DC gain, and (iii) the loop gain continues to roll off for frequencies beyond $3\omega_0$. If a pure gain is considered for the compensator, that is, $K(s) = k$, and $|P_s| = 1 \text{ MW}$, then the loop gain is

$$\ell(s) = K(s)G(s)F(s)|P_s| = (168k) \frac{s^2 + 1131^2}{s(s^2 + 2262s + 1131^2)}.$$

For $\omega \leq \omega_0/10$, the phase of $\ell(j\omega)$ is almost constant at -90° , corresponding to a phase margin of 90° . For ω larger than $\omega_0/10$, due to the double real pole at $\omega = \omega_0$, the phase drops with a slope of approximately $-90^\circ/\text{dec}$. Thus, if we need a phase margin of, for example, 70° , we should select the loop gain crossover frequency, that is, ω_c , to be about 1.93 decade larger than $\omega_0/10$, that is, $\omega_c = 218 \text{ rad/s}$. Substituting for $\omega_c = 218 \text{ rad/s}$ in equation $|\ell(j\omega_c)| = 1$, we find $k = 1.40 (\text{kV})^{-1}$, for which the exact phase margin is 68° , and the closed-loop poles are located at $s = -1910 \text{ rad/s}$ and $s = -294 \pm j267 \text{ rad/s}$. Figure 7.17 shows the frequency responses of the loop gain and closed-loop transfer function. It is observed that the bandwidth of the closed-loop system is about $\omega_b = 400 \text{ rad/s}$. The closed-loop transfer function is $G_{cl}(s) = |P_s|K(s)G(s)/(1 + \ell(s))$.

⁴By definition, a proper transfer function is one whose denominator has a degree equal to or higher than that of its numerator.

8

Grid-Imposed Frequency VSC System: Control in dq -Frame

8.1 INTRODUCTION

Chapter 5 presented dynamic models for the two-level VSC in $\alpha\beta$ -frame and dq -frame and briefly discussed its control based on generic block diagrams of Figures 5.5 and 5.7. Chapter 6 introduced the three-level NPC as an extension of the two-level VSC and established that the dynamic model of the three-level NPC is identical to that of the two-level VSC, except that the three-level NPC requires a DC-side voltage equalizing system to maintain DC-side capacitor voltages, each at half the net DC-side voltage. Thus, Chapter 6 presented a unified model for the three-level NPC and the two-level VSC (Fig. 6.18 and 6.19). Chapter 7 introduced a class of VSC systems referred to as *grid-imposed frequency VSC systems*. On the basis of the unified model of Chapter 6, Chapter 7 presented $\alpha\beta$ -frame models and controls for two members of the family of the grid-imposed frequency VSC systems, namely, the *real/reactive-power controller* and the *controlled DC-voltage power port*. In parallel with Chapter 7, this chapter presents dq -frame models and controls for the real/reactive-power controller and the controlled DC-voltage power port.

As discussed in Chapter 7, compared to the abc -frame control, the $\alpha\beta$ -frame control of a grid-imposed frequency VSC system reduces the number of plants to be controlled from three to two. Moreover, instantaneous decoupled control of the real and reactive power, exchanged between the VSC system and the AC system, is possible in $\alpha\beta$ -frame. However, the control variables, that is, feedback signals, feed-forward signals, and control signals are sinusoidal functions of time. It is shown in this chapter that the dq -frame control of a grid-imposed VSC system features all merits of the $\alpha\beta$ -frame control, in addition to the advantage that the control variables are DC quantities in the steady state. This feature ~~is~~ remarkably facilitates the compensator design, especially in variable-frequency scenarios.

To achieve zero steady-state error in the $\alpha\beta$ -frame control, the bandwidth of the closed-loop system must be adequately larger than the AC system frequency; alternatively, the compensators can include complex-conjugate pairs of poles at the AC system frequency and other frequencies of interest, to increase the loop gain. In the dq -frame control, however, zero steady-state error is readily achieved by including

8.3.4 Phase-Locked Loop (PLL)

Substituting for $\vec{V}_s(t)$ from (8.4) in (8.1), we deduce

$$V_{sd} = \hat{V}_s \cos(\omega_0 t + \theta_0 - \rho), \quad (8.18)$$

$$V_{sq} = \hat{V}_s \sin(\omega_0 t + \theta_0 - \rho). \quad (8.19)$$

Thus, (8.11)–(8.13) can be rewritten as

$$L \frac{di_d}{dt} = L\omega(t)i_q - (R + r_{on})i_d + V_{td} - V_{sd}, \quad (8.20)$$

$$L \frac{di_q}{dt} = -L\omega(t)i_d - (R + r_{on})i_q + V_{tq} - V_{sq}, \quad (8.21)$$

$$\frac{d\rho}{dt} = \omega(t). \quad (8.22)$$

Based on (8.19), $\rho(t) = \omega_0 t + \theta_0$ corresponds to $V_{sq} = 0$. Therefore, we devise a mechanism to regulate V_{sq} at zero. This can be achieved based on the following feedback law:

$$\omega(t) = H(p)V_{sq}(t), \quad (8.23)$$

where $H(p)$ is a linear transfer function (compensator) and $p = d(\cdot)/dt$ is a differentiation operator. Substituting for V_{sq} from (8.19) in (8.23), and substituting for ω from (8.23) in (8.22), we deduce

$$\frac{d\rho}{dt} = H(p)\hat{V}_s \sin(\omega_0 t + \theta_0 - \rho). \quad (8.24)$$

Equation (8.24) describes a nonlinear dynamic system, which is referred to as PLL [49], [78–80]. The function of the PLL is to regulate ρ at $\omega_0 t + \theta_0$. However, in view of its nonlinear characteristic, the PLL can exhibit unsatisfactory behavior under certain conditions. For example, if the PLL starts from an initial condition corresponding to $\rho(0) = 0$ and $\omega(0) = 0$, then the term $\hat{V}_s H(p) \sin(\omega_0 t + \theta_0 - \rho)$ in (8.24) is a sinusoidal function of time with frequency ω_0 . Then, if $H(s)$ has a low-pass frequency response, the right-hand side of (8.24) and also $d\rho/dt$ exhibit small sinusoidal perturbations about zero, the PLL falls in a limit cycle, and ρ does not track $\omega_0 t + \theta_0$. To prevent the limit cycle from taking place, the control law can be modified as

$$\omega(t) = H(p)V_{sq}(t), \quad \omega(0) = \omega_0 \quad \text{and} \quad \omega_{min} \leq \omega \leq \omega_{max}, \quad (8.25)$$

where $\omega(t)$ has the initial value $\omega(0) = \omega_0$ and is limited to the lower and upper limits of, respectively, ω_{min} and ω_{max} . ω_{min} and ω_{max} are selected to be close to ω_0 and thus to define a narrow range of variations for $\omega(t)$. On the other hand, the range of

each to provide 45° at 200 rad/s. Thus,

$$F(s) = \left(\frac{s + (p/\alpha)}{s + p} \right) \left(\frac{s + (p/\alpha)}{s + p} \right), \quad (8.33)$$

where

$$p = \omega_c \sqrt{\alpha} \quad (8.34)$$

$$\alpha = \frac{1 + \sin \delta_m}{1 - \sin \delta_m}, \quad (8.35)$$

and δ_m is the phase of each lead compensator at ω_c . If $\delta_m = 45^\circ$, based on (8.33)–(8.35), we calculate $F(s)$ as

$$F(s) = \left(\frac{s + 83}{s + 482} \right)^2. \quad (8.36)$$

Substituting for $F(s)$ from (8.36) in (8.32), we deduce

$$\ell(s) = \frac{h (s^2 + 568,516) (s^2 + 166s + 6889)}{s^2 (s^2 + 1508s + 568,516) (s^2 + 964s + 232,324)}. \quad (8.37)$$

It then follows from $|\ell(j200)| = 1$ and $\hat{V}_{sn} = 391$ V that $h = 2.68 \times 10^5$. Therefore, $h/\hat{V}_{sn} = 685.42$ and the final compensator is

$$H(s) = \frac{685.42 (s^2 + 568,516) (s^2 + 166s + 6889)}{s (s^2 + 1508s + 568,516) (s^2 + 964s + 232,324)} \quad [(\text{rad/s})/\text{V}]. \quad (8.38)$$

Figure 8.6 depicts the frequency response of $\ell(j\omega)$ based on the compensator of (8.38). It is observed that $|\ell(j\omega)|$ drops with the slope of -40 dB/dec, for $\omega \ll \omega_c = 200$. However, around ω_c the slope of $|\ell(j\omega)|$ reduces to about -20 dB/dec and $\angle \ell(j\omega)$ rises to about -120° at $\omega = \omega_c$, corresponding to a phase margin of 60° . Figure 8.6 also illustrates that $|\ell(j\omega)|$ continues to drop with a slope of -40 dB/dec for $\omega > \omega_c$. This characteristic is desired as the AC components of V_{sq} due to the harmonic distortion of V_{sabc} are attenuated. In particular, at $\omega = 6\omega_0$, $|\ell(j\omega)|$ is about -30 dB.

Figure 8.7 illustrates the start-up transient of the PLL. Figure 8.7 shows that, initially, from $t = 0$ to $t = 0.07$ s the compensator output is saturated at $\omega_{min} = 2\pi \times 55$ rad/s and, therefore, V_{sd} and V_{sq} vary with time. At about $t = 0.07$ s, V_{sq} crosses zero and intends to become negative. Thus, $H(s)$ increases ω to regulate V_{sq} at zero. Figure 8.7 indicates that V_{sq} is regulated at zero within 0.15 s. It should be noted that if ω_{min} is selected closer to ω_0 , the start-up transient period becomes shorter. However, ω_{min} cannot be selected too close to ω_0 since the PLL would not be able to quickly react to other types of disturbance.

becomes positive thereafter

0.02

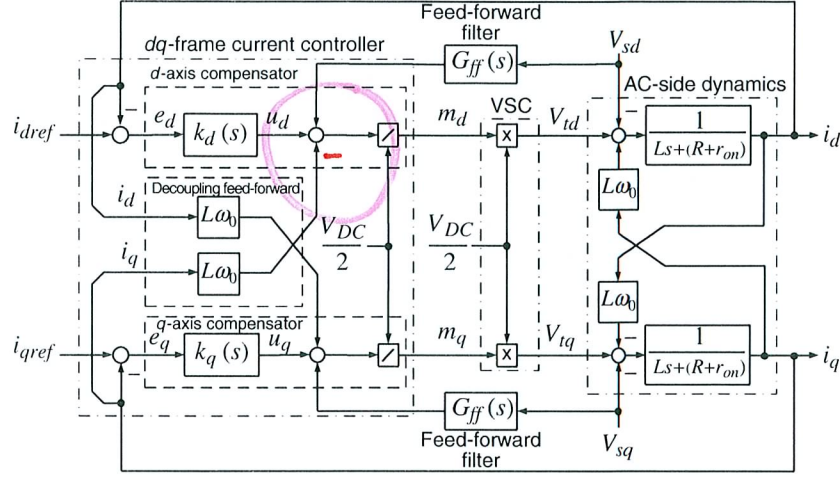


FIGURE 8.10 Control block diagram of a current-controlled VSC system.

V_{tq} from the resultant in (8.45) and (8.46), we deduce

$$L \frac{di_d}{dt} = -(R + r_{on})i_d + u_d, \quad (8.51)$$

$$L \frac{di_q}{dt} = -(R + r_{on})i_q + u_q. \quad (8.52)$$

Equations (8.51) and (8.52) describe two decoupled, first-order, linear systems. Based on (8.51) and (8.52), i_d and i_q can be controlled by u_d and u_q , respectively. Figure 8.10 shows a block representation of the d - and q -axis current controllers of the VSC system in which u_d and u_q are the outputs of two corresponding compensators. The d -axis compensator processes $e_d = i_{dref} - i_d$ and provides u_d . Then, based on (8.49), u_d contributes to m_d . Similarly, the q -axis compensator processes $e_q = i_{qref} - i_q$ and provides u_q that, based on (8.50), contributes to m_q . The VSC then amplifies m_d and m_q by a factor of $V_{DC}/2$ and generates V_{td} and V_{tq} that, in turn, control i_d and i_q based on (8.45) and (8.46). On the basis of the above-mentioned control process, one can sketch the simplified control block diagram of Figure 8.11, which is equivalent to the control system of Figure 8.10. It should be noted that in the control system of Figure 8.10, all the control, feed-forward, and feedback signals are DC quantities in the steady state.

Figure 8.11 indicates that the control plants in both d - and q -axis current-control loops are identical. Therefore, the corresponding compensators can also be identical. Consider the d -axis control loop. Unlike the $\alpha\beta$ -frame control where the compensators are fairly difficult to optimize and typically are of high dynamic orders, $k_d(s)$ can be a simple proportional-integral (PI) compensator to enable tracking of a DC reference

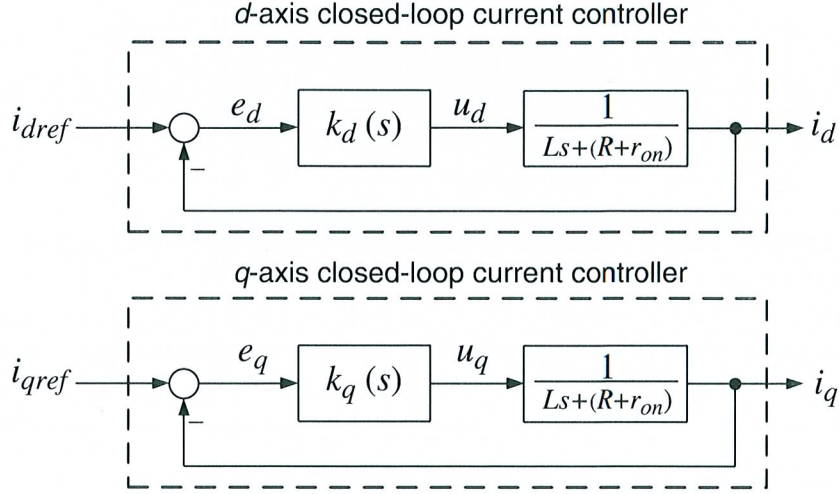


FIGURE 8.11 Simplified block diagram of the current-controlled VSC system of Figure 8.10.

command. Let

$$k_d(s) = \frac{k_p s + k_i}{s}, \quad (8.53)$$

where k_p and k_i are proportional and integral gains, respectively. Thus, the loop gain is

$$\ell(s) = \left(\frac{k_p}{Ls} \right) \frac{s + k_i/k_p}{s + (R + r_{on})/L}. \quad (8.54)$$

It is noted that due to the plant pole at $s = -(R + r_{on})/L$, which is fairly close to the origin, the magnitude and the phase of the loop gain start to drop from a relatively low frequency. Thus, the plant pole is first canceled by the compensator zero $s = -k_i/k_p$, and the loop gain assumes the form $\ell(s) = k_p/(Ls)$. Then, the closed-loop transfer function, that is, $\ell(s)/(1 + \ell(s))$, becomes

$$\frac{\overline{I_q(s)}}{\overline{I_{qref}(s)}} = \frac{I_d(s)}{I_{dref}(s)} = G_i(s) = \frac{1}{\tau_i s + 1}, \quad (8.55)$$

if

$$k_p = L/\tau_i, \quad (8.56)$$

$$k_i = (R + r_{on})/\tau_i. \quad (8.57)$$

where τ_i is the time constant of the resultant closed-loop system.

8.4.2 Selection of DC-Bus Voltage Level

As discussed in Sections 7.3.4, 7.3.5, and 7.3.6, the DC-bus voltage of the real-/reactive-power controller of Figure 8.3 must satisfy the following criteria:

$$V_{DC} \geq 2\hat{V}_t, \quad \text{PWM}, \quad (8.58)$$

$$V_{DC} \geq 1.74\hat{V}_t, \quad \text{PWM with third-harmonic injection}. \quad (8.59)$$

Thus, one must properly evaluate \hat{V}_t under the worst-case operating condition. Since the VSC system controls P_s and Q_s , \hat{V}_t should also be expressed in terms of P_s and Q_s . Based on (8.45) and (8.46), and under the assumptions that $V_{sq} = 0$ and $(R + r_{on}) \approx 0$, we deduce

$$V_{td} = L \frac{di_d}{dt} - L\omega_0 i_q + V_{sd}, \quad (8.60)$$

$$V_{tq} = L \frac{di_q}{dt} + L\omega_0 i_d. \quad (8.61)$$

Substituting for i_d and i_q from (8.41) and (8.42) in (8.60) and (8.61), and assuming that V_{sd} is constant, we obtain

$$V_{td} = \left(\frac{2L}{3V_{sd}} \right) \frac{dP_s}{dt} + \left(\frac{2L\omega_0}{3V_{sd}} \right) Q_s + V_{sd}, \quad (8.62)$$

$$V_{tq} = - \left(\frac{2L}{3V_{sd}} \right) \frac{dQ_s}{dt} + \left(\frac{2L\omega_0}{3V_{sd}} \right) P_s. \quad (8.63)$$

Based on (4.77), the amplitude of the AC-side terminal voltage is

$$\hat{V}_t = \sqrt{V_{td}^2 + V_{tq}^2}. \quad (8.64)$$

Furthermore, the amplitude of the modulating signal is

$$\hat{V}_t = \hat{m} \frac{V_{DC}}{2}. \quad (8.65)$$

As discussed in Section 7.3.6, if the conventional PWM is employed, \hat{m} can assume a value up to unity, whereas with the PWM with third-harmonic injection, \hat{m} can be as large as 1.15.

To calculate the maximum of \hat{V}_t , consider the following worst-case scenario. Initially, the system is under a steady-state condition, that is, $P_s = P_{sref} = P_{s0}$ and $Q_s = Q_{sref} = Q_{s0}$. At $t = t_0$, P_{sref} and Q_{sref} are subjected to step changes from P_{s0} to $P_{s0} + \Delta P_s$, and Q_{s0} to $Q_{s0} + \Delta Q_s$, respectively. As discussed in Section 8.4.1,

As (8.41) and (8.42) indicate, P_s and Q_s are directly related to I_d and I_q , respectively (assuming that V_{sd} is constant). Thus, based on (8.55),

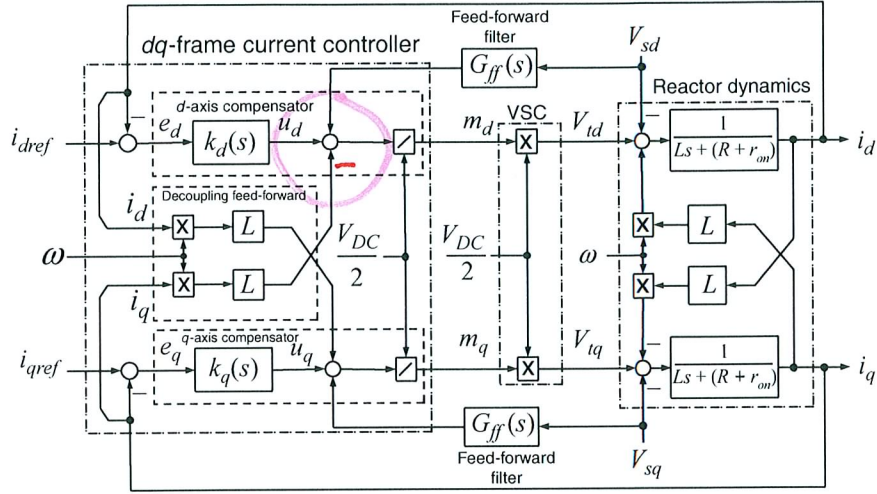


FIGURE 9.2 Control block diagram of a current-controlled VSC system.

where τ_i is a design parameter, then d - and q -axis closed-loop transfer functions assume the forms

$$I_d(s) = G_i(s)I_{dref}(s) = \frac{1}{\tau_i s + 1} I_{dref}(s), \quad (9.4)$$

$$I_q(s) = G_i(s)I_{qref}(s) = \frac{1}{\tau_i s + 1} I_{qref}(s). \quad (9.5)$$

It is noted that τ_i turns out to be the time constant of the first-order, closed-loop, transfer functions. With reference to Figure 9.1, dynamics of the load voltage are described by state-space equations:

$$C_f \frac{dV_{sa}}{dt} = i_a - i_{La}, \quad (9.6)$$

$$C_f \frac{dV_{sb}}{dt} = i_b - i_{Lb}, \quad (9.7)$$

$$C_f \frac{dV_{sc}}{dt} = i_c - i_{Lc}. \quad (9.8)$$

Equations (9.6)–(9.8) constitute the space-phasor equation

$$C_f \frac{d\vec{V}_s}{dt} = \vec{i} - \vec{i}_L. \quad (9.9)$$

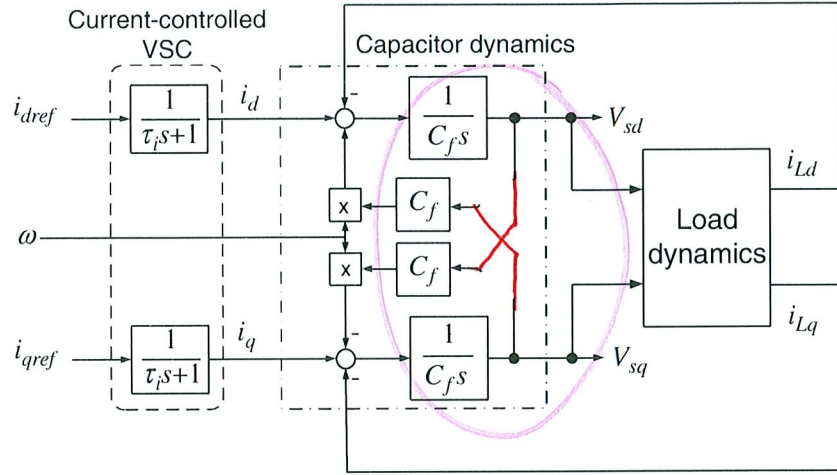


FIGURE 9.3 Block diagram of the load voltage dynamic model.

dynamic order of the load model depend on the load configuration and the number of storage elements².

EXAMPLE 9.1 Dynamic Model of a Series *RL* Load

Assume that the load in the system of Figure 9.1 is a three-phase series *RL* branch (Fig. 9.4). With reference to Figure 9.4, we have

$$\begin{aligned} L_1 \frac{di_{1a}}{dt} &= -R_1 i_{1a} + V_{sa} - V_{n1}, \\ L_1 \frac{di_{1b}}{dt} &= -R_1 i_{1b} + V_{sb} - V_{n1}, \\ L_1 \frac{di_{1c}}{dt} &= -R_1 i_{1c} + V_{sc} - V_{n1}, \end{aligned} \quad (9.16)$$

Equation (9.16) is equivalent to

$$L_1 \frac{d\vec{i}_1}{dt} = -R_1 \vec{i}_1 + \vec{V}_s. \quad (9.17)$$

²The exception is an ideal, independent, current-sourced load for which i_{Ld} and i_{Lq} are independent of V_{sd} , V_{sq} , and ω .

In some applications, T_{ext} does not depend (or depends weakly) on ω_r or θ_r and therefore can be regarded as a disturbance input to the control system. However, in most energy conversion applications, T_{ext} is a function of ω_r , θ_r , and other exogenous variables. For example, in a wind turbine T_{ext} is a nonlinear function of the machine rotor speed, wind speed, and turbine pitch angle. If the pulsating torque of a horizontal-axis wind turbine is also considered, then T_{ext} is also a nonlinear function of the rotor position, θ_r . In general,

$$T_{ext} = f(\omega_r, \theta_r, u_1, \dots, u_n), \quad (10.12)$$

where u_1, \dots, u_n are exogenous variables. Equations (10.7)–(10.12) describe an electromechanical system consisting of the machine and the mechanical system. Equations (10.7)–(10.9) correspond to the machine electrical dynamics whereas (10.10)–(10.12) describe the mechanical system. The electrical equations can be made decoupled from those of the mechanical system if participation of θ_r in (10.7)–(10.9) is compensated. As such, the electromechanical system can be divided into two subsystems: the electrical subsystem for which \vec{V}_s and \vec{V}_r are the control inputs and T_e is the output, and the mechanical subsystem for which T_e is the control input. Depending on the application, ω_r , θ_r , or the mechanical power $P_m = T_{ext}\omega_r$ can be defined as the output. In this chapter, we concentrate on the control of T_e by the VSC system.

10.3.1 Asynchronous Machine

10.3.1.1 Machine Model in Rotor-Field Coordinates In this section, we present the controls for the VSC system of Figure 10.1 that is interfaced with an asynchronous machine. We consider a squirrel-cage asynchronous machine or, equivalently, a wound-rotor asynchronous machine whose rotor terminals are short circuited and rotor current is not measurable. Thus, in (10.7)–(10.9), $\vec{V}_r = 0$ and \vec{i}_r is not measurable.

Let us introduce the fictitious space phasor current $\vec{i}_{mr} = \hat{i}_{mr} e^{j\rho}$ and the change of variable $(1 + \sigma_r) e^{j\theta_r} \vec{i}_r + \vec{i}_s = \vec{i}_{mr}$, [43]. Then, we have

$$(1 + \sigma_r) \vec{i}_r + e^{-j\theta_r} \vec{i}_s = \hat{i}_{mr} e^{j(\rho - \theta_r)}. \quad (10.13)$$

Solving for \vec{i}_r in (10.13), we deduce

$$\vec{i}_r = \frac{\hat{i}_{mr} e^{j\rho} - \vec{i}_s}{1 + \sigma_r} e^{-j\theta_r}. \quad (10.14)$$

it should be noted that T_{eref} is often either the output of another compensator or the product of an inherent feedback loop. An example of the former is a variable-speed motor drive where T_{eref} is determined by a speed (or position) control loop that regulates ω_r (or θ_r). An example of the latter is a variable-speed wind-power unit where T_{eref} is set to be proportional to ω_r^2 . In both cases, ω_r is related to T_e and thus the loop is closed.

The flux regulator and torque controller parts of Figure 10.4 issue the commands i_{sdref} and i_{sqref} which, in turn, control i_{sd} and i_{sq} based on an inherently, nonlinear, two-input-two-output system. The next subsection shows that by proper control and feed-forward compensation techniques, one can transform the system into two decoupled, single-input-single-output (SISO), linear time-invariant subsystems, each characterized by a first-order transfer function, $G_i(s)$ (Fig. 10.4); one subsystem relates i_{sd} to i_{sdref} whereas the other subsystem relates i_{sq} to i_{sqref} . We will also show that by proper selection of parameters of (d - and q -axis) compensators, one can make the time constant of $G_i(s)$ arbitrarily small.

10.3.1.3 Machine Current Control by VSC System As discussed in the previous subsection, the machine flux and torque are controlled, respectively, by i_{sd} and i_{sq} . However, the VSC can only control the stator voltage.³ Therefore, one must first develop mathematical expressions to relate i_{sd} and i_{sq} to V_{sd} and V_{sq} .

The stator terminal voltage and current are related based on (10.1) and (10.3). Substituting for \vec{i}_r from (10.14) in (10.3), and then for $\vec{\lambda}_s$ from the resultant in (10.1), we obtain

$$L_m \frac{d}{dt} \left[\frac{(1 + \sigma_s)(1 + \sigma_r) - 1}{1 + \sigma_r} \vec{i}_s + \frac{1}{1 + \sigma_r} \hat{i}_{mr} e^{j\rho} \right] = \vec{V}_s - R_s \vec{i}_s. \quad (10.23)$$

Defining the machine total leakage factor, σ , as [43]

$$\sigma = 1 - \frac{1}{(1 + \sigma_r)(1 + \sigma_s)}, \quad (10.24)$$

we can rewrite (10.23) as

$$L_m \sigma (1 + \sigma_s) \frac{d \vec{i}_s}{dt} + L_m (1 - \sigma) (1 + \sigma_s) \frac{d}{dt} (\hat{i}_{mr} e^{j\rho}) = \vec{V}_s - R_s \vec{i}_s. \quad (10.25)$$

Dividing both sides of (10.25) by R_s , we deduce

$$\sigma \tau_s \frac{d \vec{i}_s}{dt} + (1 - \sigma) \tau_s \frac{d}{dt} (\hat{i}_{mr} e^{j\rho}) = \frac{1}{R_s} \vec{V}_s - \vec{i}_s, \quad (10.26)$$

³The VSC can directly control the stator current if a hysteresis-band current-control strategy is employed rather than the PWM strategy. The main disadvantage of the method is the variable switching frequency.

Calculating the derivative in (11.11), multiplying both sides by $e^{j\theta}$, and decomposing the resultant into real and imaginary components, we obtain

$$V_{sd} = L_g \frac{di_{gd}}{dt} - L_g \omega i_{gq} + \hat{V}_g \cos(\omega_0 t + \theta_0 - \rho), \quad (11.15)$$

$$V_{sq} = L_g \frac{di_{gq}}{dt} + L_g \omega i_{gd} + \hat{V}_g \sin(\omega_0 t + \theta_0 - \rho), \quad (11.16)$$

where $\omega = d\rho/dt$. As detailed in Section 8.3.4, ω is controlled by the PLL (Fig. 8.5), based on the control law

$$\frac{d\rho}{dt} = \omega(t) = H(p)V_{sq}(t), \quad (11.17)$$

where $p = d(\cdot)/dt$ is the differentiation operator and $H(s)$ is the transfer function of the PLL compensator. Thus, $H(p)f(t)$ ($f(t)$ is an arbitrary function of time) represents the zero-state response of $H(s)$ to the input $f(t)$. As explained in Section 8.3.4, the PLL compensator includes one integral term and thus $\omega(t)$ assumes a nonzero steady-state value when V_{sq} settles at zero. Equations (11.13)–(11.17) represent a dynamic system for which V_{sd} is the output, i_d and i_q are the control inputs, and i_{Ld} and i_{Lq} are the disturbance inputs. The system is nonlinear due to the presence of the terms $\hat{V}_g \cos(\omega_0 t + \theta_0 - \rho)$ and $\hat{V}_g \sin(\omega_0 t + \theta_0 - \rho)$. Moreover, the frequency of the VSC system, ω , is a dynamic variable that depends on the operating point. To further clarify this point, let us substitute for V_{sq} , from (11.16), in (11.17):

$$\frac{d\rho}{dt} = L_g H(p) \left(\frac{di_{gq}}{dt} + \omega i_{gd} \right) + \hat{V}_g H(p) \sin(\omega_0 t + \theta_0 - \rho). \quad (11.18)$$

Equation (11.18) indicates that dynamic responses of ρ and ω , in addition to their natural transient components corresponding to $i_{gd} = i_{gq} = 0$, include forced components that are functions of i_{gd} and i_{gq} . This is in contrast to the case of a stiff grid described by (8.24). Based on (8.24), if the VSC is interfaced with a stiff AC system, the responses of ρ and ω merely include natural transient components; the PLL dynamics are decoupled from those of the rest of the system and the operating point and, therefore, once the PLL reaches the steady state, $\rho = \omega_0 t + \theta_0$ and $\omega = \omega_0$.

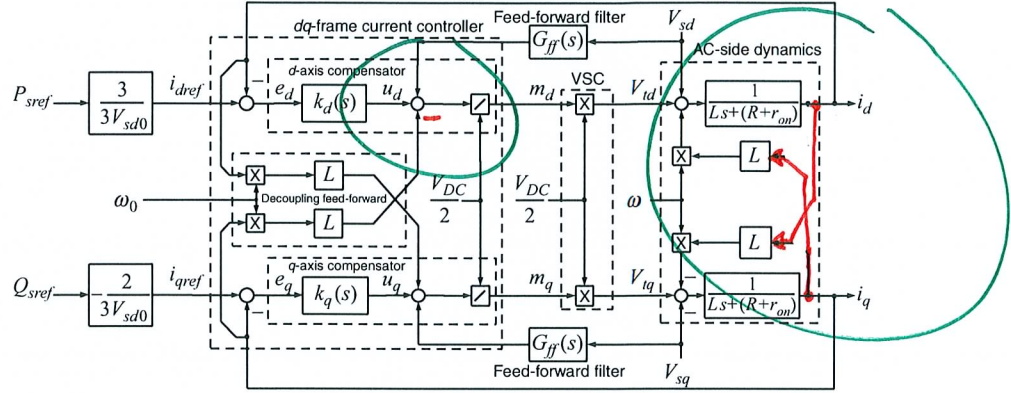


FIGURE 11.5 Control block diagram of the STATCOM dq -frame current controller (see Section 8.4.1 for details).

approach as the one adopted for the controlled DC-voltage power port (Section 8.6). In contrast, however, in the STATCOM Q_s , which is usually a free control variable in the controlled DC-voltage power port, is controlled through a closed-loop mechanism that regulates the PCC voltage. The PCC voltage regulation is based on the model of Figure 11.2 or its simplified version (Fig. 11.4). Since $V_{sq} = 0$, the control of P_s and Q_s is equivalent to the control of i_d and i_q , respectively (see equations (4.83) and (4.84)).

The structure of the VSC dq -frame current controller shown in Figure 8.10, is repeated here as Figure 11.5. There is, however, a minor difference between the control systems of Figures 8.10 and 11.5: if the AC system is stiff, the PLL dynamics are decoupled from those of the other system variables. Thus, once the PLL start-up transients are passed, the angular velocity of the dq -frame settles to the constant value ω_0 . This condition holds for the current controller of Figure 8.10, where $\omega = \omega_0$ appears as a constant parameter in both the plant coupling terms and the controller decoupling terms. However, in the case of the STATCOM, ω is a dynamic variable in the plant model, as illustrated in Figure 11.5; this is due to the AC system weakness and the PLL dynamics. Thus, to decouple the plant d - and q -axis dynamics, theoretically, ω (that is, an output of the PLL) should be used in the controller decoupling terms, rather than ω_0 . However, accepting a suboptimal (but quite effective) decoupling, we use ω_0 in the STATCOM current-control scheme, as shown in Figure 11.5.

With reference to Figure 11.5, compensators $k_d(s)$ and $k_q(s)$ are

$$k_d(s) = k_q(s) = \frac{k_p s + k_i}{s}. \quad (11.45)$$

fault. As Figure 12.20(a) shows, during the fault V_{sabc1} is unbalanced. However, due to feed-forward of V_{sd1} and V_{sq1} (see Fig. 12.8), i_{abc1} remains balanced (Fig. 12.20(b)). Moreover, since P_{sref1} is not changed during the faults period, i_{d1} remains constant. Therefore, since $\hat{i}_1 = \sqrt{i_{d1}^2 + i_{q1}^2}$ and $i_{q1} = 0$, the amplitude of i_{abc1} does not change with respect to the prefault condition, as Figure 12.20(b) illustrates. Figure 12.20(c) and (d) shows that V_{sabc2} and i_{abc2} are balanced since PCC2 is sound. However, to maintain the balance of (average) real power, the DC-bus voltage controller reduces the absolute value of P_{s2-act} from 24 to 16 MW (see Fig. 12.19(b)), through the reduction of the amplitude of i_{abc2} (Fig. 12.20(d)).

Figure 12.21 illustrates the same variables shown in Figure 12.20, but for the case where PCC2 is subjected to the line-to-ground fault. In this case, V_{sabc1} and i_{abc1} remain unchanged with respect to the prefault condition, whereas V_{sabc2} is unbalanced. However, in contrast to the case of the fault at PCC1, the amplitude of i_{abc2} increases following the fault inception (Fig. 12.21(d)). The reason is that during the fault at PCC2, the DC component of P_{s2-act} remains equal to the prefault value of P_{s2-act} as shown in Figure 12.19(b). However, the amplitude of the positive-sequence component of V_{sabc2} drops due to the imbalance. Consequently, to transfer the same average power as the prefault condition, i_{abc2} is increased proportionally by the DC-bus voltage controller.

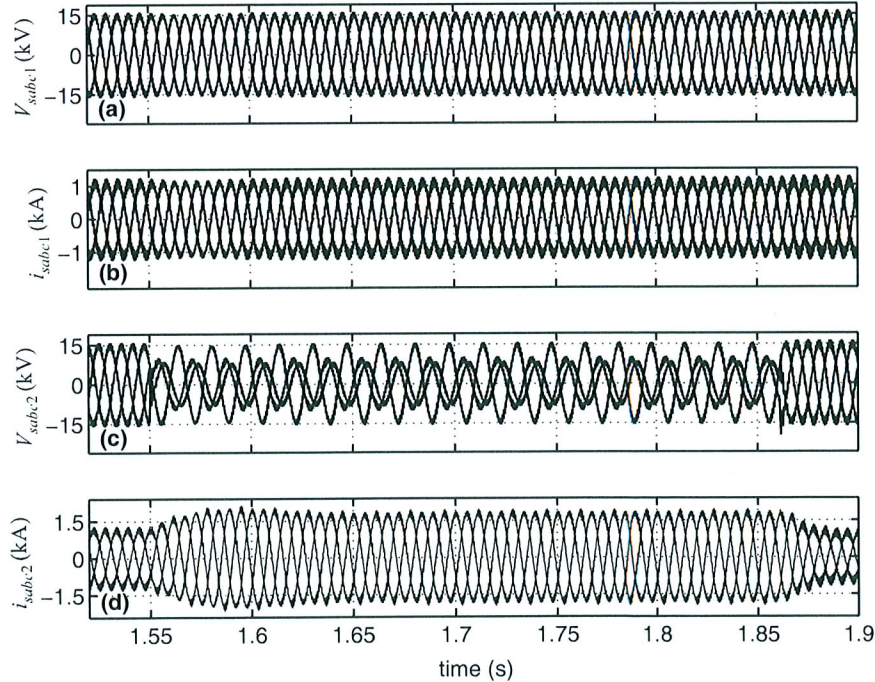


FIGURE 12.21 Line current and PCC voltage waveforms of the HVDC system of Figure 12.1 when the fault occurs at PCC2.

for which the parameter τ is 0.066 s. The explanations of the flux observer and its parameters are given in Section 10.3.2. The variable-frequency VSC system also has an embedded dq -frame current controller (Fig. 10.17) whose compensator $k(s)$ has the transfer function

$$k(s) = 15.23 \frac{s + 21.86}{s}.$$

For the controlled DC-voltage power port of the wind-power system, that is, Figure 13.11, we have

$$K_V(s) = 299.66 \frac{(s + 19.18)}{s(s + 2083)} \quad [\Omega^{-1}],$$

$$\frac{I_{dref2}(s)}{P_{sref2}(s)} = \frac{2}{3\hat{V}_{s2}} = 1.361 \quad [(\text{kV})^{-1}],$$

$$\frac{I_{qref2}(s)}{Q_{sref2}(s)} = \frac{-2}{3\hat{V}_{s2}} = -1.361 \quad [(\text{kV})^{-1}].$$

The commands i_{dref2} and i_{qref2} are handed to the dq -frame current-control scheme of Figure 8.10, which employs the compensators $k_d(s)$ and $k_q(s)$, as

$$k_d(s) = k_q(s) = 0.764 \frac{s + 28.84}{s} \quad [\Omega].$$

Moreover, the transfer function of the feed-forward filters of the current controller is

$$G_{ff}(s) = \frac{1}{8 \times 10^6 s + 1}.$$

8×10^{-6}

The transfer function of the compensator $H(s)$ of the PLL (Fig. 13.10(a)) is

$$H(s) = \frac{142,680(s^2 + 568,516)(s^2 + 166s + 6889)}{s(s^2 + 1508s + 568,516)(s^2 + 964s + 232,324)} \quad [(\text{rad/s})/\text{kV}].$$

Under the nominal grid voltage and with i_{rd} set to zero, the machine reactive power is $Q_{s1} = 400$ kVAr, based on (10.116). The filter capacitor C_f delivers a reactive power of $Q_f = 49.8$ kVAr. Therefore, to fulfill the operation of the wind-power system at unity power factor, the AC/DC/AC converter system is required to deliver a reactive power of 350.2 kVAr to the grid. Since the variable-frequency VSC system and the controlled DC-voltage power port necessarily handle equal amounts of real power, the reactive power of 350.2 kVAr should

Multiplying both sides of (A.9), (A.10), and (A.11), respectively, by $(2/3)e^{j0}$, $(2/3)e^{j2\pi/3}$, and $(2/3)e^{j4\pi/3}$, adding the resultants, and employing the definition of the space phasor based on (4.2), we deduce

$$\vec{\lambda}_s = L_s \vec{i}_s + L_m e^{j\theta_r} \vec{i}_r, \quad (\text{A.12})$$

where

$$\begin{aligned} L_s &= L_{ss} - M_{ss}, \\ L_m &= \left(\frac{2}{3} \right) M_{sr}. \end{aligned} \quad (\text{A.13})$$

(Handwritten note: The fraction 2/3 in the equation above is crossed out and replaced with 3/2 in red ink.)

A.3.3 Rotor Flux Space Phasor

Similarly, the flux linked by the rotor windings can be formulated as

$$\begin{aligned} \lambda_{ra} &= L_{rr}i_{ra} + M_{rr}i_{rb} + M_{rr}i_{rc} \\ &+ M_{sr} \cos(\theta_r) i_{sa} + M_{sr} \cos\left(\theta_r - \frac{2\pi}{3}\right) i_{sb} + M_{sr} \cos\left(\theta_r + \frac{2\pi}{3}\right) i_{sc}, \end{aligned} \quad (\text{A.14})$$

$$\begin{aligned} \lambda_{rb} &= M_{rr}i_{ra} + L_{rr}i_{rb} + M_{rr}i_{rc} \\ &+ M_{sr} \cos\left(\theta_r + \frac{2\pi}{3}\right) i_{sa} + M_{sr} \cos(\theta_r) i_{sb} + M_{sr} \cos\left(\theta_r - \frac{2\pi}{3}\right) i_{sc}, \end{aligned} \quad (\text{A.15})$$

$$\begin{aligned} \lambda_{sc} &= M_{rr}i_{ra} + M_{rr}i_{rb} + L_{rr}i_{rc} \\ &+ M_{sr} \cos\left(\theta_r - \frac{2\pi}{3}\right) i_{sa} + M_{sr} \cos\left(\theta_r + \frac{2\pi}{3}\right) i_{sb} + M_{sr} \cos(\theta_r) i_{sc}, \end{aligned} \quad (\text{A.16})$$

where L_{rr} and M_{rr} are the self- and mutual inductances, respectively. Due to the symmetry of the magnetic structure, L_{rr} and M_{rr} are constant parameters. However, the mutual inductance between a rotor winding and a stator winding is a function of the rotor angle θ_r , as discussed in Section A.3.2. Multiplying both sides of (A.14), (A.15), and (A.16), respectively, by $(2/3)e^{j0}$, $(2/3)e^{j2\pi/3}$, and $(2/3)e^{j4\pi/3}$, adding the resultants, and employing the definition of the space phasor based on (4.2), we deduce

$$\vec{\lambda}_r = L_r \vec{i}_r + L_m e^{-j\theta_r} \vec{i}_s, \quad (\text{A.17})$$

where

$$L_r = L_{rr} - M_{rr}, \quad (\text{A.18})$$

and L_m is defined by (A.13).

$$T_e = \left(\frac{3}{2} L_m \right) \text{Im} \left\{ \vec{i}_s \vec{i}_r'^* \right\}, \quad (\text{A.25})$$

where $\omega_r = d\theta_r/dt$ is the rotor angular velocity. The term $j\omega_r \vec{\lambda}_r'$ in (A.22) represents a voltage component, proportional to the rotor speed, which can be regarded as the rotor back EMF.

Let us define the rotor and stator leakage factors as

$$\sigma_s = \frac{L_s}{L_m} - 1, \quad (\text{A.26})$$

$$\sigma_r = \frac{L_r}{L_m} - 1. \quad (\text{A.27})$$

Then, (A.23) and (A.24) can be rewritten as

$$\vec{\lambda}_s = \sigma_s L_m \vec{i}_s + L_m \underbrace{(\vec{i}_r' + \vec{i}_s)}_{\vec{i}_m}, \quad (\text{A.28})$$

$$\vec{\lambda}_r' = \sigma_r L_m \vec{i}_r' + L_m \underbrace{(\vec{i}_r' + \vec{i}_s)}_{\vec{i}_m}, \quad (\text{A.29})$$

Based on (A.3), (A.22), (A.28), and (A.29), Figure A.2 presents an equivalent circuit for the machine. The equivalent circuit of Figure A.2 is known as the *air-gap flux model* or the *T-form model* of the machine [109]. The equivalent circuit of Figure A.2 represents the squirrel-cage asynchronous machine, if \vec{V}_r' is zero. In the doubly-fed asynchronous machine, in addition to \vec{V}_s , the rotor voltage vector \vec{V}_r' is also controllable. The equivalent circuit of Figure A.2 is valid for both dynamic and steady-state conditions.

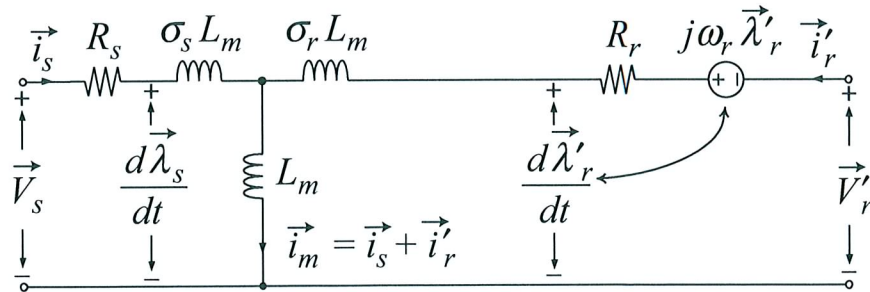


FIGURE A.2 Space-phasor domain equivalent circuit of the symmetrical three-phase machine.